Lawrence Berkeley National Laboratory
LBL Publications

Title

EELS Studies of Cerium Electrolyte Reveal Substantial Solute Concentration Effects in Graphene Liquid Cells

Permalink

https://escholarship.org/uc/item/0z41s573

Journal

Journal of the American Chemical Society, 145(12)

ISSN

0002-7863

Authors

Crook, Michelle F
Moreno-Hernandez, Ivan A
Ondry, Justin C
et al.

Publication Date

2023-03-29

DOI

10.1021/jacs.2c07778

Peer reviewed

EELS studies reveal in-situ oxidation of concentrated cerium electrolyte substantially influences the chemical environment in graphene liquid cells

Michelle F. Crook,[†] Ivan A. Moreno-Hernandez,[†] Justin C. Ondry,[†,‡] Jim Ciston,[¶] Karen C. Bustillo,[¶] Alfred Vargas,[§] and A. Paul Alivisatos[*,†,‡,‖,⊥,#]

[†]Department of Chemistry, University of California, Berkeley, California 94720, United States

[‡]Kavli Energy NanoScience Institute, Berkeley, California 94720, United States

[¶]National Center for Electron Microscopy Facility, Molecular Foundry, Lawrence Berkeley National Laboratory, Berkeley, California 94720, United States

[§]Department of Chemical and Biomolecular Engineering, University of California, Berkeley, California 94720, United States

[‖]Materials Sciences Division, Lawrence Berkeley National Laboratory, Berkeley, California 94720, United States

[⊥]Department of Materials Science and Engineering, University of California, Berkeley, California 94720, United States

[#]Present Address: Department of Chemistry, University of Chicago, Chicago IL 60637, United States

E-mail: paul.alivisatos@uchicago.edu

Abstract

Abstract

Graphene liquid cell transmission electron microscopy is a powerful technique to visualize nanoscale dynamics and transformations at atomic resolution. However, the solution in liquid cells is known to be affected by radiolysis, and the stochastic formation of graphene liquid cells raises questions about the solution chemistry in individual pockets. In this study, electron energy loss spectroscopy (EELS) was used to evaluate a model encapsulated solution, aqueous $CeCl_3$. First, the ratio between the O K-edge and Ce M-edge was used to approximate the concentration of cerium salt in the graphene liquid cell. It was determined that the ratio between oxygen and cerium was orders of magnitude lower than what is expected for a dilute solution, indicating that the encapsulated solution is highly concentrated. To probe how this affects the chemistry within graphene liquid cells, the oxidation of Ce^{3+} was measured using time-resolved parallel EELS. It was determined that Ce^{3+} oxidizes faster under high electron fluxes, but reaches the same steady state Ce^{4+} concentration regardless of flux. The time-resolved concentration profiles enabled direct comparison to radiolysis models, which indicate rate constants and g-values of certain molecular species are substantially different in the highly-concentrated environment. Finally, electron flux-dependent gold nanocrystal etching trajectories showed that gold nanocrystals etch faster at higher electron fluxes, correlating well with the Ce^{3+} oxidation kinetics. Understanding the effects of the highly-concentrated solution in graphene liquid cells will provide new insight on previous studies, and may open up opportunities to systematically study systems in highly-concentrated solutions at high resolution.

Introduction

Liquid cell transmission electron microscopy (LCTEM) is a technique that allows users to study systems at nanoscale resolution in solution. This technique has uncovered many dis-

coveries such as new mechanisms of growth and etching of nanocrystals,[1–5] nanocrystalline structure in solution,[6,7] and nanocrystal superlattice formation.[8–11] This technique will continue to generate active interest because, thus far, it is the only method that enables the direct structural observation of single particle trajectories of nanocrystal chemical transformations. From the beginning, there have been concerns that the observation conditions would not correspond to that of the native colloidal solution. The earliest studies showed that the effective viscosity of the trapped liquids were orders of magnitude higher than typical liquids,[2] in part because the most readily observed nanocrystals are trapped near the surface.[12] Early simulations suggested that there are significant perturbations of the liquid by the electron beam,[13] and that these perturbations significantly alter the reactivity. More recent work has shown that these effects can be modulated using redox couples.[14] This study here suggests that there is an additional major difference with common nanocrystal growth solution conditions, namely the possibility that the fluids in graphene liquid cells are highly concentrated electrolytes.

There has been significant progress over the last decade to understand the solution chemistry in LCTEM. At this point it is well known that many of the observed chemical transformations are controlled by electron beam initiated reactions. The electron beam of the TEM induces radiolysis of water molecules (or other solvents) to form highly reactive species, such as $^\bullet$OH, H$^\bullet$, H$_2$O$_2$, among others,[15–17] which can either interact directly with the sample,[18–20] or with added solutes to induce changes in the sample,[4,14,21–23] with increasing evidence that these reactive species can be deliberately controlled to explore different kinetic regimes. Yet, as the structures of the solvated species that may drive chemical transformations in the liquid cell are indiscernible with electron microscopy, work to understand the solution chemistry and it's interactions with a sample of interest has relied on models,[13] correlative experiments,[18,21,24] or through probing indirect chemical transformations.[14,22,25]

More recently, advanced TEM techniques such as electron energy loss spectroscopy (EELS) have been used to determine changes in the sample upon irradiation. EELS is a

technique in which electrons from the electron beam scatter inelastically within the sample, losing characteristic amounts of energy that correspond to inner shell or valence transitions.[26] Through analysis of the fine structure of the energy loss spectrum of core transitions, information such as oxidation state and chemical environment can be inferred. EELS has been used in conjunction with LCTEM previously to measure the thickness of the liquid,[27,28] or to check for water by confirming the presence of the O K-edge.[28–30] If the liquid layer is sufficiently thin, fine structure analysis of core-loss transitions can be performed through the liquid.[31] This has been done previously to explore how irradiation in LCTEM changes the oxidation states of materials,[32,33] and even to measure the water structure in liquid cells.[34–36]

In this study, we use core-loss EELS to elucidate the solution chemistry present in graphene liquid cells. Graphene liquid cells are a particularly interesting liquid cell type, as they are easy to prepare, do not require a specialized holder, and the thin, low-Z graphene windows offer the highest resolution of the liquid cell configurations. With graphene liquid cells, a solution of interest is placed between two graphene coated TEM grids, and the van der Waals forces between the graphene sheets hermetically seal a small volume of the solution and protect it from the vacuum environment of the TEM.[37] While graphene liquid cells have been utilized to study systems at high resolution, the nature of these liquid cells raise questions about the solution chemistry and how it may differ from bulk solutions. It has been suggested that 2D materials such as graphene exert a van der Waals pressure on liquid or gas molecules trapped between layers,[38–40] and this phenomenon has been suggested to occur in graphene liquid cells as well.[41] Additionally, the individual pockets within a graphene liquid cell form stochastically, sometimes around objects like nanocrystals,[42] indicating that the environment could differ from region to region. Finally, since these pockets form through evaporative drying of the solution, the concentration of species within the liquid cell may be different from the original encapsulating solution.

Here, we use EELS to probe the chemistry of a model redox couple, Ce^{3+}/Ce^{4+}, in graphene liquid cells. The Ce^{3+}/Ce^{4+} redox couple was chosen as Ce has a large EELS cross

section, there are marked differences between the Ce^{3+} and Ce^{4+} EEL spectra, and previous work has shown that this redox couple has the potential to etch gold nanocrystals in graphene liquid cells. Steady-state EELS results indicated that the solution within graphene liquid cells was substantially more concentrated than the preparation solution across various starting concentrations. As a highly concentrated solution likely alters the kinetics of the system, we next studied the oxidation kinetics of Ce^{3+} with time-resolved EELS. The rate of oxidation of Ce^{3+} increased with increasing electron flux, but all systems reached a similar steady-state Ce^{4+} concentration regardless of electron flux. It was determined that the kinetics of oxidation could not be explained with prior radiolysis models derived from pulse radiolysis results of dilute solutions. The radiolysis models were revised to account for the observed Ce^{3+} oxidation kinetics, largely through methods developed for highly concentrated solutions. These factors indicate that the graphene liquid cell technique results in a substantial increase in the concentration of solutes, and for the studies conducted herein the solution may be better described as a hydrated salt matrix rather than a dilute liquid solution. Lastly, we studied the electron flux dependent etching of gold nanocrystals, a model system, and correlated the results to the kinetic EELS data.

Experimental Section

Nanocrystal Synthesis: Gold nanocrystals were synthesized following a modified procedure published previously.[43]

Preparation of Au Seeds: Briefly, 5 mL of 100 mM cetyltrimethylammonium ammonia chloride (CTAC) and 0.25 mL of 10 mM hydrochloroauric acid ($HAuCl_4$) were added to a clean, 20 mL vial. The vial was put into a water bath set to 30 °C and was stirred rapidly. Gold seeds were formed by adding 0.45 mL of 20 mM $NaBH_4$. The dispersion was allowed to stir for 1 minute, then left undisturbed at 30 °C for 1.5 hr to decompose any excess $NaBH_4$.

Preparation of Nanocrystals: Two identical solutions of 4.5 mL of 100 mM CTAC, 0.25

mL of 10 mM $HAuCl_4$, and 90 μL of 40 mM ascorbic acid were each added to clean 20 mL vials, in order. To the first vial, 1 mL of the seed solution was added during rapid stirring until the solution turned pale pink (approximately 5 s). Then, 12.5 μL of this solution was added into the other vial, briefly mixed, and left to sit on the bench for 15 mins to allow the growth to complete. The solution was then washed and resuspended in water three times by centrifugation at 8000 rpm for 10 minutes. After the final washing, the nanocrystals were concentrated to an OD of 1, then stored in a vial in the dark.

Graphene Liquid Cell Preparation: Graphene liquid cells were prepared as described previously[37] with modifications as follows. The encapsulating solutions were prepared as follows: a 100 mM solution of $CeCl_3$ was prepared with 0.1 M HCl. The encapsulating solution was prepared by adding 100 μL of the metal salt solution and 100 μL of water to a small vial. Nanocrystals were introduced by adding 10 μL of the nanocrystal solution to the encapsulating solution just before assembly of the graphene liquid cell for a final $CeCl_3$ concentration of 40 mM in the encapsulating solution. Approximately 0.5 μL of the encapsulating solution was placed on the graphene side of a graphene coated grid held in self-closing tweezers. A half-grid, prepared by cutting a grid with a razor, was then immediately placed graphene side down on top of the droplet and left to dry for 10 minutes.

Electron Energy Loss Spectroscopy (EELS): All EELS experiments were performed in parallel-beam mode on the TEAM I double-corrected S/TEM microscope at the National Center for Electron Microscopy, Molecular Foundry, Lawrence Berkeley National Laboratory (LBNL). The microscope was operated at 300 kV with a high brightness 'X-FEG' electron source. A Gatan Continuum Imaging Filter with a 2.5 mm entrance aperture was used in conjunction with a K3 IS direct electron detector operated in electron-counting mode to collect the spectra. A source monochromator was used to obtain an energy resolution of approximately 0.25 eV. All data was collected in Dual EELS mode to capture the low loss and high loss regions simultaneously with the ZLP-lock function engaged to align spectra before summing to remove jitter in the elastic energy. The collection angle for all experiments

was 25 mrad, set by a 100 μm objective aperture. The electron fluxes were calibrated on the camera. A custom script was used to control the microscope conditions (magnification, C2 lens %, etc.) when each spectra was acquired. The size of the irradiated area was then measured on the camera and determined to have a diameter of approximately 100 nm. All EELS analysis was performed in Python using custom scripts. All background subtraction was performed in Hyperspy using a power law model.

Time resolved EELS: The steps for collecting the time resolved EELS data are as follows. First, a suitable liquid pocket containing a gold nanocrystal was identified using low magnification and low electron flux (<1 e$^-$Å^{-2}s^{-1}) imaging conditions. Using a custom script, the microscope beam was blanked, then switched to a high magnification setting at the desired electron flux (125-500 e$^-$Å^{-2}s^{-1}) where only a region approximately 100 nm in diameter was irradiated. If the nanocrystals etched, indicating that the region was wet, then the beam was blanked, and the sample was moved to a location at least a few hundred nanometers away, outside the initial irradiated region. The EELS time series data collection feature in Digital Micrograph was initiated, then the beam was unblanked to ensure that the first electrons hitting the sample were collected in the time series. The time series were collected at 10 spectra per second for 2 minutes. A custom script was used to deconvolve the Ce^{3+} and Ce^{4+} contributions in each spectrum of the time series. More information on this script is provided in the SI.

***In Situ* TEM Imaging:** All BF-TEM videos were collected on a FEI Tecnai T-20 S-Twin TEM operating at 200 kV with a LaB$_6$ filament. *In situ* videos were collected with a Gatan Rio 16 IS camera using the Digital Micrograph *in situ* data collection function. Videos were binned by two for a 2048 $\times$ 2048 pixel area. The nominal magnification for all videos was 145 kx for a pixel resolution of 0.92 Å/pixel. The frame rate for all videos was either 4 or 10 fps, yielding a temporal resolution of 0.25 and 0.1 s, respectively. To convert counts to electrons, a conversion value of 124 counts/electron (provided by the manufacturer) was used. The electron flux was calibrated using a custom script[22] and checked several times

throughout a session to maintain accuracy. When searching for nanocrystals, the electron flux was kept low (<15 e$^-$Å^{-2}s^{-1}) to prevent electron-beam induced reactions prior to video collection.

Radiolysis Chemical Network Model: A literature kinetic model was adjusted based on the EELS data collected herein on the kinetics of Ce^{3+} oxidation during graphene LCTEM imaging. The model is based on the MATLAB code written by Schneider et al., which implements a kinetic model by Elliot and McCracken.[13,44] The model includes previously reported reactions between species derived from water, chloride, and cerium.[13,14,45] For more information on the model, see the SI.

Results and Discussion

It has recently become clear that metal nanocrystal etching studies in LCTEM have been controlled by redox processes of metal ions in solution. It is suggested that preloaded metal ions are oxidized under electron beam irradiation by radiolytically produced hydroxyl radicals.[14,21] This oxidized species then has the electrochemical potential to oxidize the metal nanocrystals in solution, a process which can be captured in real time in the TEM. This redox cycling process can be inferred based on *in situ* TEM observations, yet direct evidence is lacking.

By using parallel-beam EELS, direct chemical insight into these transformations can be obtained, while irradiating the sample with the same conditions used in metal nanocrystal etching studies. In this work, we used EELS to gain experimental insight into the chemistry of the solution in graphene liquid cells (Figure 1a). Previous work has shown that the Ce^{3+}/Ce^{4+} redox couple is a suitable beam-initiated etchant for gold nanocrystals.[14] This system allows *in situ* observation of gold nanocrystal etching as preloaded CeCl$_3$ is oxidized to a Ce^{4+} species, forming a Ce^{3+}/Ce^{4+} redox couple with an electrochemical potential sufficiently positive to spontaneously etch gold nanocrystals (Figure 1b). Additionally, Ce^{3+}

and Ce^{4+} have sharp $M_{4,5}$ edge white lines, which makes Ce readily identifiable with EELS. Further, Ce^{3+} and Ce^{4+} have distinct differences in fine structure, which can be seen in the spectra of the solid state standards for Ce^{3+} and Ce^{4+}, CeF_3 and CeO_2, respectively (Figure 1c). This enables chemical identification of the Ce oxidation state using EELS, making the Ce redox couple a suitable model system for determining electron beam-initiated transformations in graphene liquid cells. The M-edge of Ce^{3+} has two major peaks at 881.6 and 898.9 eV, as well as smaller features at 880.8, 895.9 and 897.5 eV. The M-edge of Ce^{4+} has two major peaks at slightly higher energies at 883.0 and 900.8 eV, as well as two satellite peaks at 888.3 and 906.0 eV that originate from the LMCT between the Ce metal center and the ligands.[46,47] For these reasons, we use EELS to study the Ce^{3+}/Ce^{4+} redox couple etching gold nanocrystals as a model system to probe the solution chemistry in graphene liquid cells.

The liquid pockets of a graphene liquid cell are typically formed through an evaporative drying process to seal the top and bottom graphene sheets together,[37,48] and it is possible that this may increase the concentration of species in solution. This is in contrast to another well-developed liquid cell geometry, the SiN liquid cell, where a hermetic seal is formed between o-rings and the SiN chips, meaning that evaporation is not necessary for the seal to form, and the solution in graphene liquid cells may be more concentrated than the SiN liquid cells. To measure the concentration of the encapsulated solution in graphene liquid cells, gold nanocrystals were added to the $CeCl_3$ solution and irradiated to induce etching before collecting an EEL spectrum. This is to confirm that the area under measurement was consistent with typical behavior observed in previous liquid cell studies.[14] Additionally, the irradiated area in these measurements was intentionally limited to a relatively small area (see Experimental) to attempt to fully capture liquid regions in these spectra. EELS was used to approximate the concentration of graphene liquid cells by taking the ratio of the oxygen K-edge and cerium M-edge signals and their respective cross sections for each measurement. In this system, oxygen is only present in water, and any oxygen coming from
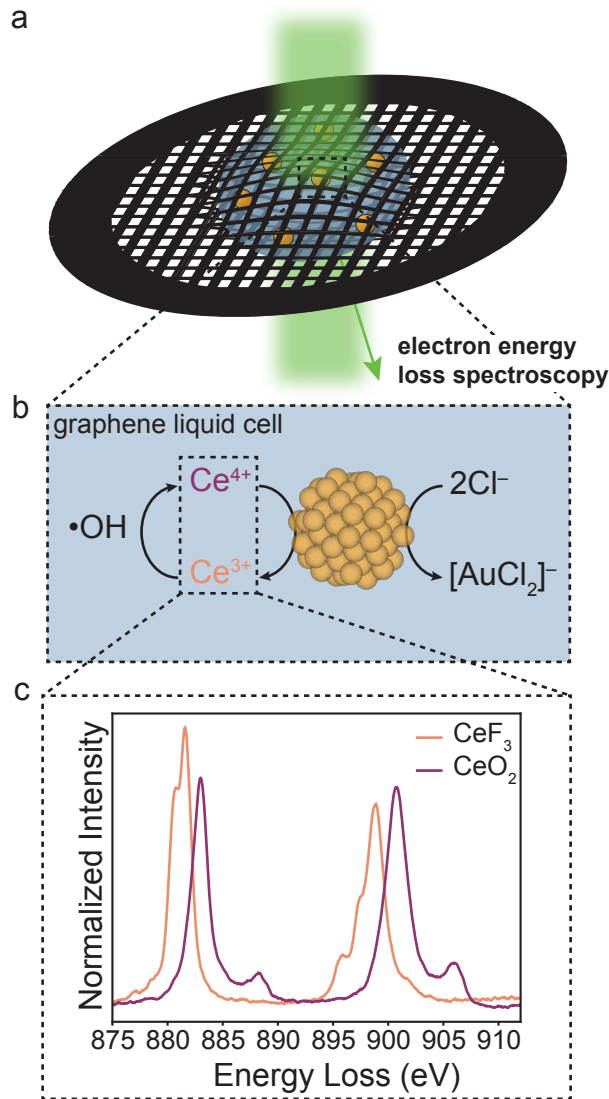
Figure 1: a) Schematic of a graphene liquid cell irradiated with an electron beam. b) Schematic of the proposed redox reactions occurring at the gold nanocrystal surface during electron beam initiated etching. c) Electron energy loss spectra of the Ce M-edge for CeF_3 (Ce^{3+}) and CeO_2 (Ce^{4+}). Note the distinct differences in the fine structure with the change in oxidation state.

the grid should be negligible (see Figure S 1). We first measured the oxygen to cerium ratio for graphene liquid cells prepared with 40 mM $CeCl_3$, which is the same order of magnitude of oxidant used previously in etching studies.[3,4,14,21,22,25] Figure 2a shows a representative spectrum collected from these graphene liquid cells (bottom), while Figure 2b shows the box plot of the measurements (right). The average oxygen to cerium ratio measured for the 40 mM solution is 3.46 ± 2.72. In a 40 mM $CeCl_3$ solution, the ratio of oxygen to cerium atoms is approximately 1300 to 1. Additionally, the solubility limit of $CeCl_3$ in water is approximately 4 M, which corresponds to an oxygen to cerium ratio of 14 to 1. The ratios measured are significantly lower than what is expected, and also lower than the maximum solubility of a $CeCl_3$ solution. While it is possible that parts of the irradiated region were dry which could lower the measured ratio, the measured ratio is still three orders of magnitude lower than what is expected for a dilute solution. The lateral dimensions of the graphene liquid cell pockets are typically larger than the irradiated region used in these experiments, on the order of several hundred nanometers or more, (see Figure S 2 and[29,49]) indicating that it is likely that a significant portion of the irradiated region is hydrated. Further, time resolved thickness measurements and time resolved oxygen to cerium ratio measurements indicate that the solution is not evaporating upon exposure to the electron beam (see Figure S 3 and Figure S 4). Ultimately, while it is possible that the measurements underestimate the amount of water present, it is clear that the encapsulated solution is substantially more concentrated than the original solution.

Although the solution of the graphene liquid cells measured herein indicate that the encapsulated solution is highly concentrated, it may be possible to decrease the concentration of the encapsulated solution by preparing the graphene liquid cells with increasingly dilute initial solutions. We next prepared graphene liquid cells made with 4 mM and 0.4 mM $CeCl_3$. Gold nanocrystals were added to the initial solution, but we were unable to induce etching of the gold nanocrystals in most cases of graphene liquid cells prepared with 4 mM $CeCl_3$ and in all cases of the graphene liquid cells prepared with 0.4 mM $CeCl_3$. Representative

11

spectra collected from these graphene liquid cells are shown in Figure 2a and box plots of the calculated oxygen to cerium ratios are shown in Figure 2b. The average oxygen to cerium ratio measured for the graphene liquid cells prepared with 4 mM and 0.4 mM $CeCl_3$ are 4.1 $\pm$1.9, and 20.9 $\pm$10.7, respectively. This data indicates that it is possible to create a more dilute solution in graphene liquid cells by preparing a more dilute initial solution, although the encapsulated solutions are, for the most part, still quite concentrated. When we prepared graphene liquid cells with 0.4 mM $CeCl_3$, the most dilute region we found had an oxygen to cerium ratio of 212 to 1, which corresponds to a concentration of approximately 260 mM. Beginning with a dilute initial solution appears to increase the chances of encapsulating a moderately dilute solution, yet there is still significant variability of the measured oxygen to cerium ratios across the initial concentrations and individual grids measured (see Figure S 5). Nevertheless, the purpose of this study is to understand the effects of the solution on gold nanocrystal etching in graphene liquid cells. In this context, reproducible etching trajectories of gold nanocrystal seem to occur in regions where the encapsulated solution is highly concentrated. Further discussion of the concentration of the solution, including Raman and EDS data, can be found in the SI and Figure S 6, Figure S 7, and Figure S 8.

The high concentration of salt in the encapsulated solution in graphene liquid cells may have important implications for the kinetics of the chemical transformations in the solution. To probe this, we used time resolved EELS to study the oxidation of Ce^{3+} in a solution of 40 mM $CeCl_3$ and gold nanocrystals. Select spectra of a representative EELS time series collected at 375 e$^-$Å^{-2}s^{-1} is shown in Figure 3a. Qualitatively, the initial spectrum is very similar to the Ce^{3+} standard spectrum, but the four features corresponding to the Ce^{4+} standard spectrum (dashed lines) as described above quickly develop. To ascertain how much Ce^{4+} is produced at each time step, a custom spectral deconvolution code was used to calculate the relative amount of Ce^{3+} and Ce^{4+} in each of these spectra (see SI for more details). In the first spectra at 0.1 s, there is approximately 9 % Ce^{4+} present in the graphene liquid cell (Figure 3c) and by 100.1 s there is 38 % Ce^{4+} present (Figure 3b). The percentage
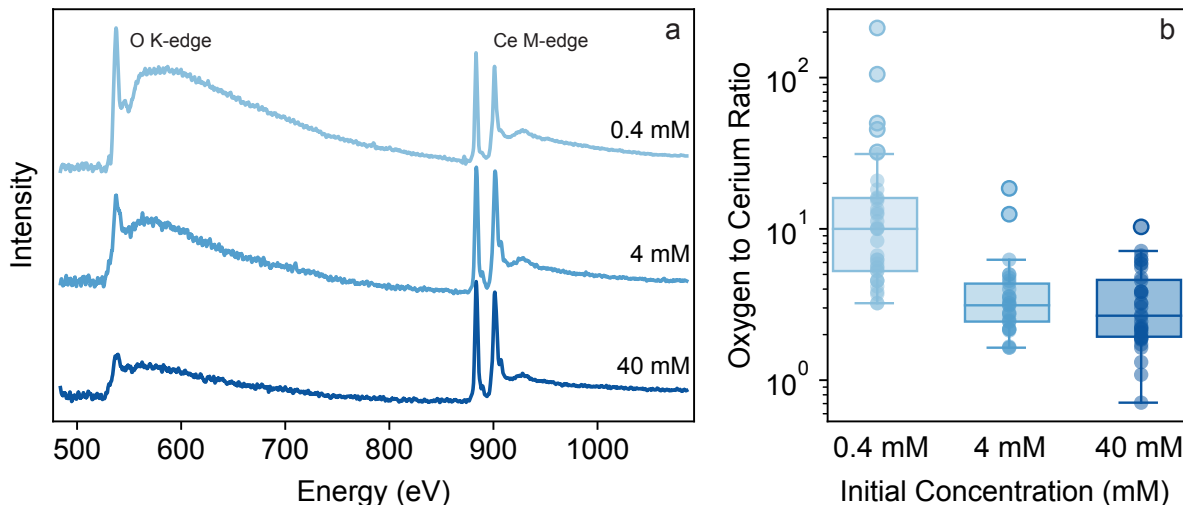
Figure 2: a) EELS core-loss and of graphene liquid cells prepared with a 0.4, 4, and 40 mM CeCl$_3$ solution. Note that the spectra are normalized to the Ce M-edge intensity to illustrate the varying amounts of oxygen present. b) Box plots of the ratio of the oxygen to cerium signals across the three different concentrations of encapsulating solutions used to prepare graphene liquid cells. The shaded region is the interquartile range of the data, the line in the box is the average, the end points of the whiskers are the range of the data, and outlined scatter point are outliers.

of Ce^{4+} was calculated for each of the $\sim$1200 spectra in the time series. By assuming that the average solution is CeCl$_3$·7H$_2$O, a known hydrated cerium salt with an oxygen to cerium ratio within range of what was measured in Figure 2, these percentages can be converted to a concentration. A plot of the Ce^{4+} concentration over time is shown in Figure 3d. The initial increase in the Ce^{4+} concentration is very fast, followed by a slower increase until reaching a steady state concentration. The Ce^{4+} formation can be modeled with an empirical biexponential function with good fit (Figure 3d).

To gain further insight into the kinetics of formation of Ce^{4+} in the graphene liquid cell, approximately 60 different time series were captured at four different electron fluxes across several samples. The time-dependent Ce^{4+} concentration was calculated for each spectrum in the time series. Plots of the Ce^{4+} concentration over time at each of the four electron fluxes in shown in Figure 4 a-d. The dark line is the average Ce^{4+} concentration at each electron flux, while the shaded region is the standard deviation of all the time series. While
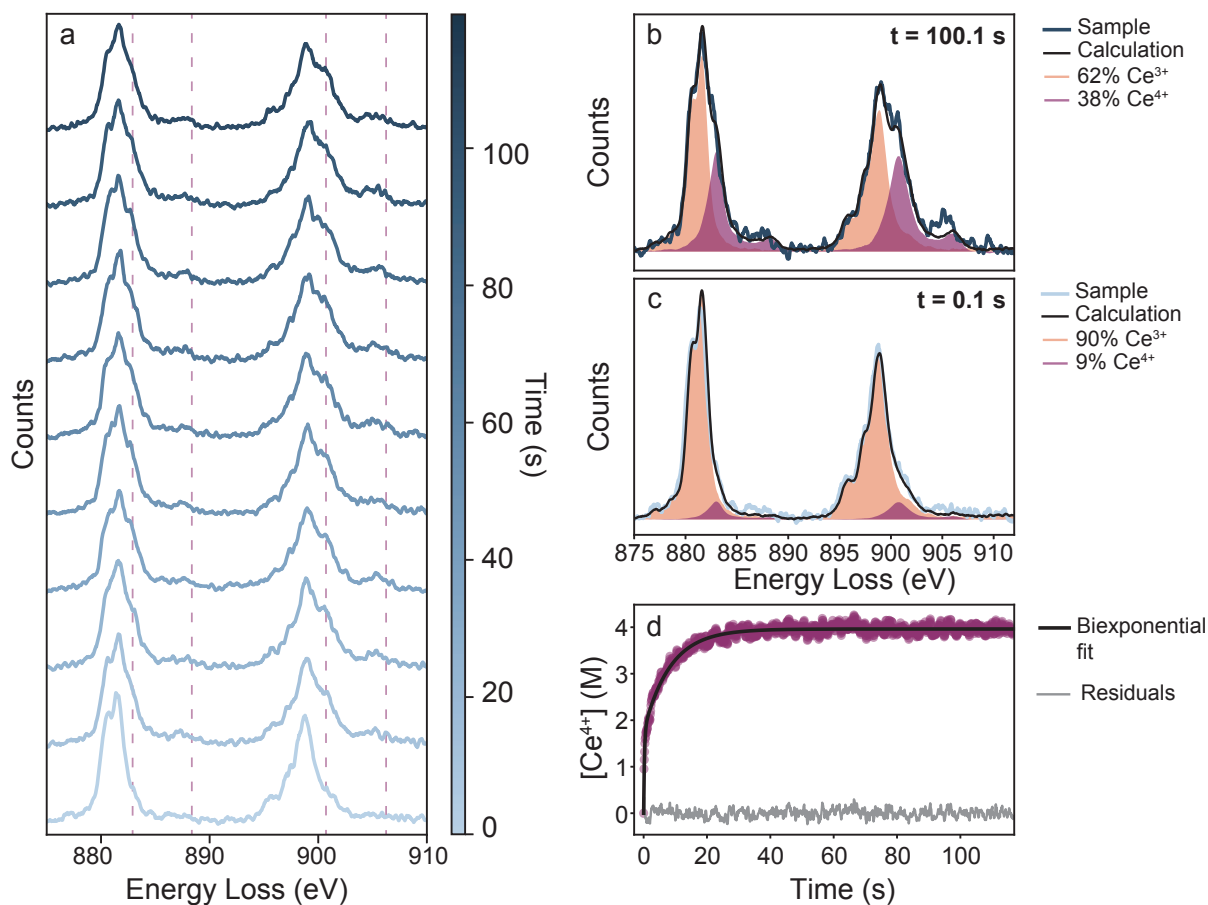
13

Figure 3: a) Time resolved EEL spectra of the Ce $M_{4,5}$ edge upon electron irradiation. Dashed lines indicate the features for Ce^{4+}. Deconvolution of the spectra taken at b) t=100.1s and c) t=0.1s indicating the relative contribution of Ce^{3+} and Ce^{4+} in each spectrum. d) Plot of the measured Ce^{4+} concentration for each spectra in the time series and the biexponential fit using the function $[Ce^{4+}] = A(1-e^{(-k_1 t)}) + B(1-e^{(-k_2 t)})$.

there is a large spread in Ce^{4+} concentration at a specific electron flux, the average steady state concentration of Ce^{4+} at each electron flux is similar (Figure 4e). To extract more information out of these curves, each individual time series was fit to the following empirical biexponential function

$$[Ce^{4+}] = A(1 - e^{(-k_1 t)}) + B(1 - e^{(-k_2 t)}) \qquad (1)$$

where A and B are the total amount of Ce^{4+} formed through the fast and slow process, respectively, and k_1 and k_2 are the rate constants for the fast and slow process, respectively. Analysis of the fitting terms reveals that as the electron flux is increased, k_1 increases (Figure 4f). This indicates that at early times, the Ce^{4+} concentration increases faster at higher electron fluxes. See Figure S 9 for the other fitting terms.

To better understand how Ce^{4+} is formed in the graphene liquid cell, we used a radiolysis model derived from pulse radiolysis studies. This model included the generation of chemical species from electron-water interactions and homogeneous reactions between water-derived species and Ce or Cl species.[13,14] More information on this model is included in the SI, Figure S 10, and Figure S 11. The initial concentration of Ce was set to 10.57 M, the molarity of cerium in $CeCl_3 \cdot 7H_2O$, which corresponds to the chemical species most closely matching the oxygen to cerium ratio observed with EELS and EDS. The model included dose partitioning between the solute and the solvent, which is required for models of highly concentrated solutions.[45] The results from this model insufficiently captured the observed Ce^{3+} oxidation kinetics, as indicated by the underestimation of the amount of Ce^{4+} generated (See Figure S 12). A sensitivity analysis of the reaction rate constants was performed to understand which reactions result in the discrepancy between experiment and theory (See Figure S 13 and Figure S 14). The sensitivity analysis indicated that the reaction rate constant between Ce^{3+} and hydroxyl radicals had to be over an order of magnitude faster to account for the experimental results (see Eq. 2), while all other rate constants remained the same. It is

expected that the increase in reactivity between hydroxyl radicals and Ce^{3+} is due to most of the water being ligated with Ce^{3+} in the graphene liquid cell, and thus the hydroxyl radicals generated through radiolysis are in close proximity to the Ce^{3+} cation and react more readily. While this could be one potential explanation for this effect, more work is needed to understand the mechanism of Ce^{3+} oxidation.

$$Ce^{3+} + {}^\bullet OH \longrightarrow Ce^{4+} + OH^-; k = 2.27 \times 10^9 \qquad (2)$$

The radiolysis model was also used to elucidate the variability in steady-state Ce^{4+} concentration observed between samples. Previous work indicates that the g-value of H_2 changes as a solution becomes significantly concentrated.[50–52] Our simulations indicate that the steady-state concentration of Ce^{4+} is strongly dependent on the g-value of H_2. Simultaneous fitting of the radiolysis model including the changes described above to the experimental data resulted in an average H_2 g-value of 0.019 molecules/eV. G-values for H_2 in the range of 0.011 to 0.028 molecules/eV could explain the spread in steady-state Ce^{4+} concentration observed between samples (grey lines, Figure 4a-d). The updated model approximates the observed kinetics much more closely than the model for dilute solutions.

It is apparent that there are observable changes to the kinetics of Ce^{4+} formation in the graphene liquid cell under different electron fluxes. We correlated these effects with a model reaction that can be readily observed with LCTEM, the etching of gold nanocrystals by Ce^{4+} cations. A graphene liquid cell was prepared with a solution containing pre-synthesized spherical gold nanocrystals and 40 mM $CeCl_3$. Dozens of gold nanocrystal etching trajectories were collected at the four different electron fluxes. Representative etching trajectories are shown in Figure 5a-d. The outline of the nanocrystal was calculated from each frame of the gold nanocrystal etching trajectory. Then, the radius of the nanocrystal at each frame of the video was determined and plotted versus time (Figure 5e). When plotting radius versus time, the plot is linear through the majority of the etching trajectory, as the radius is propor-
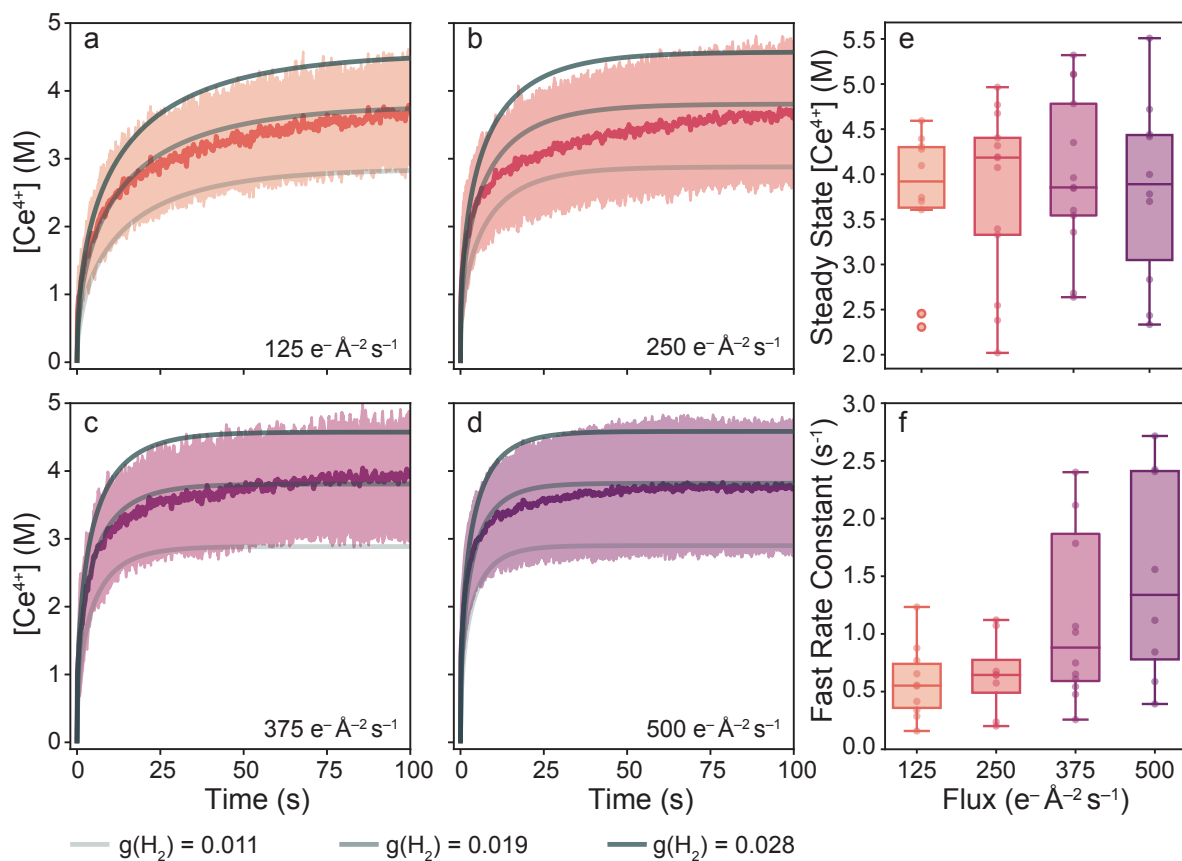
Figure 4: Average (dark line) and standard deviation (shaded region) of the measured Ce^{4+} concentration versus time at a) 125 b) 250 c) 375 and d) 500 $e^-Å^{-2}s^{-1}$. Overlaid lines are radiolytic model fits with a G-value for H_2 of 0.011 (light grey), 0.019 (grey), and 0.028 (dark grey). e) Box plots of the steady state concentration of Ce^{4+} at each of the electron fluxes. f) Box plots of the fast rate constant term at the four tested electron fluxes extracted from the biexponential fits for each time series.

tional to the surface etching rate (details of this analysis have been published previously).[14] The etch rate can then be calculated as the slope of the linear portion of the curve. The etch rate for each etching trajectory across the four electron fluxes was calculated and plotted in Figure 5f. This plot illustrates that the etch rate of gold nanocrystals increases with electron flux. Since there is substantial overlap between the time period prior to reaching steady-state Ce^{4+} concentration and time period of nanocrystal etching, it is expected that the generation rate of Ce^{4+} has an impact on the observed etching trajectories.
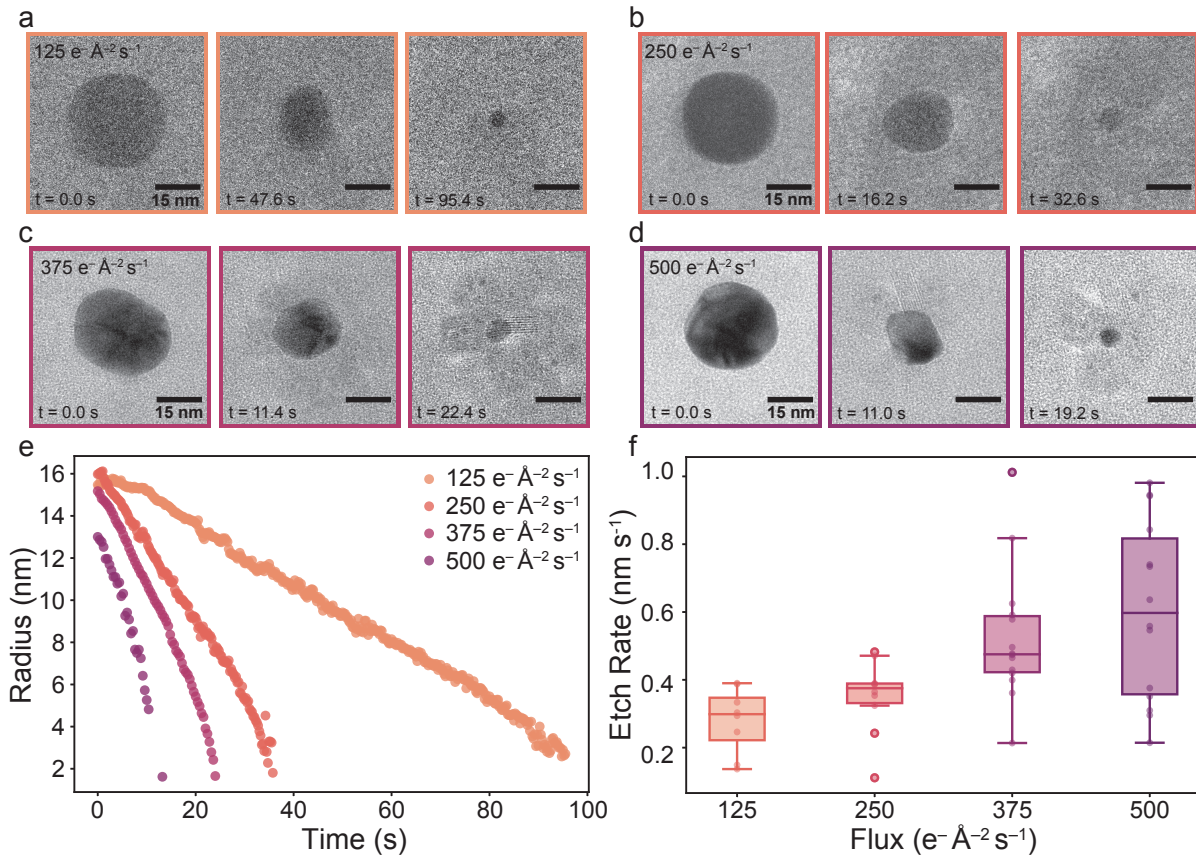
Figure 5: Etching trajectories of gold nanocrystals in a graphene liquid cell prepared with 40 mM $CeCl_3$ captured at a) 125, b) 250, c) 375, and d) 500 $e^-Å^{-2}s^{-1}$. e) Gold nanocrystal radius vs. time curves at each of the four electron fluxes. f) Box plots of the etch rates of gold nanocrystals at the four different electron fluxes.

The work presented herein suggests that graphene liquid cell solutions are significantly more concentrated compared to the original encapsulating solution. Considering this, it is possible that previously published studies using graphene liquid cells were highly con-

centrated salt solutions as well. Qualitatively, it is known that dried salt hydrates behave similarly to graphene liquid cells under the electron beam.[53] Searching the literature, it is clear that the majority of graphene liquid cell studies have used a salt solution as the encapsulating solution (see Table S 3). Studies that use organic solvents have typically used a low vapor pressure component (e.g. oleylamine), and it is possible that it remains while a high vapor pressure solvent evaporates (See Table S 4). Further, there are a few studies that claim to have encapsulated pure (e.g. deionized) water (see Table S 5), but images of liquid cells in many of these reports show high-Z or other impurities, indicating potential contamination. Empirically, it has been mentioned that trapping deionized water in graphene liquid cells is difficult,[54] and may require cleaner procedures than what is typically used for graphene liquid cell preparation for repeated success.

Moving forward, the insight obtained from this study will aid in the design and understanding of future graphene liquid cell experiments. This study highlights the importance of defining the solution in graphene liquid cells, as it can be significantly different from the prepared encapsulating solution. As shown in this work, the concentration of species can be highly concentrated, which can affect studies of chemical transformations in graphene liquid cells. Additionally, this result may impact studies of physical processes, such as dynamics and movement in graphene liquid cells. The dynamic viscosity of salt solutions increases as salinity increases,[55] which will affect the diffusion constant of nanocrystals through the Stokes-Einstein equation. Finally, care must be taken when using radiolysis models as they are designed for dilute solutions and may be inaccurate for the solutions in graphene liquid cells without further modifications specific to the graphene liquid cell environment.

Although we have shown that the nature of the encapsulated solution in graphene liquid cells have crucial differences compared to bulk solutions, these findings may be advantageous for future studies. Previous high-resolution imaging of nanocrystals in graphene liquid cells indicate that nanoscale tumbling of the particles is largely absent or significantly slowed down, which further supports that the nanocrystals are in a highly viscous medium. The

suppressed tumbling in this highly viscous medium is likely key to 3D atomic resolution tomography in liquids[6,7] and enables the observation of facet dependent reactivity under different kinetic regimes.[4] While these findings may prompt reexamination of some previous work, we expect that the improved understanding of the liquid environment we have shown here will open up new directions of graphene liquid cell research.

Conclusion

Understanding the solution chemistry in graphene liquid cells is vital to interpret the results of liquid cell experiments. In this study, EELS was used to quantify specific solution parameters. By measuring the ratio between the O K-edge and Ce M-edge in graphene liquid cells prepared with 40, 4, and 0.4 mM $CeCl_3$, it was determined that the liquid cell solution is significantly more concentrated than the initial encapsulating solution. This likely occurs during the formation process as the seal is formed through evaporation of the solvent, indicating that this effect may extend to previous graphene liquid cell studies as well. Additionally, oxidation of the Ce^{3+} metal centers were tracked using time-resolved EELS. These experiments revealed that the rate of oxidation of the Ce^{3+} metal centers is dependent on the electron flux, while the steady state concentration of Ce^{4+} is independent of electron flux. Further analysis with kinetic radiolysis models revealed that the rate of oxidation and spread in data can be rationalized by a highly concentrated solvent, with varying hydration levels in individual pockets. Finally, the flux-dependent rate of oxidation of the Ce^{3+} metal centers correlates well with the flux-dependent etching of gold nanocrystals. This study sheds new light on the nature of graphene liquid cell solutions and opens up new opportunities to study systems in dense electrolytes. The findings of this work will have implications for future graphene liquid cell experiments in a variety of fields, including chemistry, materials science, physics, and biology.

Author Information

Notes

The authors declare no competing financial interest

Acknowledgement

Supporting Information Available

The Supporting Information is available free of charge on the ACS Publications website at DOI:XXX

References

(1) Yuk, J. M.; Crommie, M. F.; Zettl, A.; Alivisatos, A. P. High Resolution EM of Colloidal Nanocrystal Growth Using Graphene Liquid Cells. *Science* **2012**, *336*.

(2) Zheng, H.; Smith, R. K.; Jun, Y.-w.; Kisielowski, C.; Dahmen, U.; Alivisatos, A. P. Observation of Single Colloidal Platinum Nanocrystal Growth Trajectories. *Science* **2009**, *324*, 1309–1312.

(3) Hauwiller, M. R.; Frechette, L. B.; Jones, M. R.; Ondry, J. C.; Rotskoff, G. M.; Geissler, P.; Alivisatos, A. P. Unraveling Kinetically-Driven Mechanisms of Gold Nanocrystal Shape Transformations Using Graphene Liquid Cell Electron Microscopy. *Nano Letters* **2018**, *18*, 5731–5737.

(4) Ye, X.; Jones, M. R.; Frechette, L. B.; Chen, Q.; Powers, A. S.; Ercius, P.; Dunn, G.; Rotskoff, G. M.; Nguyen, S. C.; Adiga, V. P.; Zettl, A.; Rabani, E.; Geissler, P.; Alivisatos, A. P. Single-particle mapping of nonequilibrium nanocrystal transformations. *Science* **2016**, *354*, 874–877.

(5) Nielsen, M. H.; Aloni, S.; De Yoreo, J. J. In situ TEM imaging of CaCO 3 nucleation reveals coexistence of direct and indirect pathways. *Science* **2014**, *345*, 1158–1162.

(6) Kim, B. H. *et al.* Critical differences in 3D atomic structure of individual ligand-protected nanocrystals in solution. *Science* **2020**, *368*, 60–67.

(7) Park, J.; Zettl, A.; Alivisatos, A. P. 3D structure of individual nanocrystals in solution by electron microscopy. *Science* **2015**, *349*, 287–290.

(8) Ou, Z.; Wang, Z.; Luo, B.; Luijten, E.; Chen, Q. Kinetic pathways of crystallization at the nanoscale. *Nature Materials* **2020**, *19*, 450–455.

(9) Wang, Y.; Peng, X.; Abelson, A.; Xiao, P.; Qian, C.; Yu, L.; Ophus, C.; Ercius, P.;

Wang, L. W.; Law, M.; Zheng, H. Dynamic deformability of individual PbSe nanocrystals during superlattice phase transitions. *Science Advances* **2019**, *5*.

(10) Park, J.; Zheng, H.; Lee, W. C.; Geissler, P. L.; Rabani, E.; Alivisatos, A. P. Direct observation of nanoparticle superlattice formation by using liquid cell transmission electron microscopy. *ACS Nano* **2012**, *6*, 2078–2085.

(11) Cepeda-Perez, E.; Doblas, D.; Kraus, T.; de Jonge, N. Electron microscopy of nanoparticle superlattice formation at a solid-liquid interface in nonpolar liquids. *Science Advances* **2020**, *6*, 1–6.

(12) Yesibolati, M. N.; Mortensen, K. I.; Sun, H.; Brostrøm, A.; Tidemand-Lichtenberg, S.; Mølhave, K. Unhindered Brownian Motion of Individual Nanoparticles in Liquid-Phase Scanning Transmission Electron Microscopy. *Nano Letters* **2020**, *20*, 7108–7115.

(13) Schneider, N. M.; Norton, M. M.; Mendel, B. J.; Grogan, J. M.; Ross, F. M.; Bau, H. H. Electron–Water Interactions and Implications for Liquid Cell Electron Microscopy. *The Journal of Physical Chemistry C* **2014**, *118*, 22373–22382.

(14) Moreno-Hernandez, I. A.; Crook, M. F.; Ondry, J. C.; Alivisatos, A. P. Redox Mediated Control of Electrochemical Potential in Liquid Cell Electron Microscopy. *Journal of the American Chemical Society* **2021**, *143*, 12082–12089.

(15) Draganić, I. G.; Draganić, Z. D. *The Radiation Chemistry of Water*; Academic Press, INC.: New York and London, 1971; pp 23–46.

(16) Allen, A. *The radiation chemistry of water and aqueous solutions.*; Van Nostrand: Princeton N.J., 1961; p 204.

(17) Schwarz, H. A. Applications of the spur diffusion model to the radiation chemistry of aqueous solutions. *The Journal of Physical Chemistry* **1969**, *73*, 1928–1937.

(18) Korpanty, J.; Parent, L. R.; Gianneschi, N. C. Enhancing and Mitigating Radiolytic Damage to Soft Matter in Aqueous Phase Liquid-Cell Transmission Electron Microscopy in the Presence of Gold Nanoparticle Sensitizers or Isopropanol Scavengers. *Nano Letters* **2021**, *21*, 1141–1149.

(19) Vratsanos, M. A.; Gianneschi, N. C. Direct Observation of Emulsion Morphology, Dynamics, and Demulsification. *ACS Nano* **2022**, *16*, 7783–7793.

(20) Gnanasekaran, K.; Korpanty, J.; Berger, O.; Hampu, N.; Halperin-Sternfeld, M.; Cohen-Gerassi, D.; Adler-Abramovich, L.; Gianneschi, N. C. Dipeptide Nanostructure Assembly and Dynamics via in Situ Liquid-Phase Electron Microscopy. *ACS Nano* **2021**, *15*, 16542–16551.

(21) Crook, M. F.; Laube, C.; Moreno-Hernandez, I. A.; Kahnt, A.; Zahn, S.; Ondry, J. C.; Liu, A.; Alivisatos, A. P. Elucidating the Role of Halides and Iron during Radiolysis-Driven Oxidative Etching of Gold Nanocrystals Using Liquid Cell Transmission Electron Microscopy and Pulse Radiolysis. *Journal of the American Chemical Society* **2021**, *143*, 11703–11713.

(22) Hauwiller, M. R.; Ondry, J. C.; Chan, C. M.; Khandekar, P.; Yu, J.; Alivisatos, A. P. Gold Nanocrystal Etching as a Means of Probing the Dynamic Chemical Environment in Graphene Liquid Cell Electron Microscopy. *Journal of the American Chemical Society* **2019**, *141*, 4428–4437.

(23) Gnanasekaran, K.; Chang, H.; Smeets, P. J. M.; Korpanty, J.; Geiger, F. M.; Gianneschi, N. C. In Situ Ni 2+ Stain for Liposome Imaging by Liquid-Cell Transmission Electron Microscopy. *Nano Letters* **2020**, *20*, 4292–4297.

(24) Touve, M. A.; Carlini, A. S.; Gianneschi, N. C. Self-assembling peptides imaged by correlated liquid cell transmission electron microscopy and MALDI-imaging mass spectrometry. *Nature Communications* **2019**, *10*, 1–12.

(25) Hauwiller, M. R.; Ye, X.; Jones, M. R.; Chan, C. M.; Calvin, J. J.; Crook, M. F.; Zheng, H.; Alivisatos, A. P. Tracking the Effects of Ligands on Oxidative Etching of Gold Nanorods in Graphene Liquid Cell Electron Microscopy. *ACS Nano* **2020**, *14*, 10239–10250.

(26) Leapman, R. *Transmission Electron Energy Loss Spectrometry in Materials Science and The EELS Atlas*; Wiley-VCH Verlag GmbH & Co. KGaA: Weinheim, FRG, 2005; pp 49–96.

(27) Keskin, S.; Kunnas, P.; de Jonge, N. Liquid-Phase Electron Microscopy with Controllable Liquid Thickness. *Nano Letters* **2019**, *19*, 4608–4613.

(28) Kelly, D. J.; Zhou, M.; Clark, N.; Hamer, M. J.; Lewis, E. A.; Rakowski, A. M.; Haigh, S. J.; Gorbachev, R. V. Nanometer Resolution Elemental Mapping in Graphene-Based TEM Liquid Cells. **2018**, *18*, 24.

(29) Sasaki, Y.; Kitaura, R.; Yuk, J. M.; Zettl, A.; Shinohara, H. Efficient preparation of graphene liquid cell utilizing direct transfer with large-area well-stitched graphene. *Chemical Physics Letters* **2016**, *650*, 107–112.

(30) Keskin, S.; Pawell, C.; de Jonge, N. Verification of water presence in graphene liquid cells. *Micron* **2021**, 103109.

(31) Holtz, M. E.; Yu, Y.; Gao, J.; Abruña, H. D.; Muller, D. A. In Situ Electron Energy-Loss Spectroscopy in Liquids. **2011**, 1027–1035.

(32) Wang, C.; Qiao, Q.; Shokuhfar, T.; Klie, R. F. High-resolution electron microscopy and spectroscopy of ferritin in biocompatible graphene liquid cells and graphene sandwiches. *Advanced Materials* **2014**, *26*, 3410–3414.

(33) Unocic, R. R.; Baggetto, L.; Veith, G. M.; Aguiar, J. A.; Unocic, K. A.; Sacci, R. L.;

Dudney, N. J.; More, K. L. Probing battery chemistry with liquid cell electron energy loss spectroscopy. *Chemical Communications* **2015**, *51*, 16377–16380.

(34) Jungjohann, K. L.; Evans, J. E.; Aguiar, J. A.; Arslan, I.; Browning, N. D. Atomic-scale imaging and spectroscopy for in situ liquid scanning transmission electron microscopy. *Microscopy and Microanalysis* **2012**, *18*, 621–627.

(35) Ghodsi, S. M.; Anand, S.; Shahbazian-Yassar, R.; Shokuhfar, T.; Megaridis, C. M. In Situ Study of Molecular Structure of Water and Ice Entrapped in Graphene Nanovessels. *ACS Nano* **2019**, *13*, 4677–4685.

(36) Jokisaari, J. R.; Hachtel, J. A.; Hu, X.; Mukherjee, A.; Wang, C.; Konecna, A.; Lovejoy, T. C.; Dellby, N.; Aizpurua, J.; Krivanek, O. L.; Idrobo, J.; Klie, R. F. Vibrational Spectroscopy of Water with High Spatial Resolution. *Advanced Materials* **2018**, *30*, 1802702.

(37) Hauwiller, M. R.; Ondry, J. C.; Alivisatos, A. P. Using Graphene Liquid Cell Transmission Electron Microscopy to Study in Situ Nanocrystal Etching. *Journal of Visualized Experiments* **2018**, 57665.

(38) Khestanova, E.; Guinea, F.; Fumagalli, L.; Geim, A. K.; Grigorieva, I. V. Universal shape and pressure inside bubbles appearing in van der Waals heterostructures. *Nature Communications* **2016**, *7*, 1–10.

(39) Vasu, K. S.; Prestat, E.; Abraham, J.; DIx, J.; Kashtiban, R. J.; Beheshtian, J.; Sloan, J.; Carbone, P.; Neek-Amal, M.; Haigh, S. J.; Geim, A. K.; Nair, R. R. Van der Waals pressure and its effect on trapped interlayer molecules. *Nature Communications* **2016**, *7*, 1–6.

(40) Lim, C. H. Y. X.; Nesladek, M.; Loh, K. P. Observing high-pressure chemistry in graphene bubbles. *Angewandte Chemie - International Edition* **2014**, *53*, 215–219.

(41) Ghodsi, S. M.; Sharifi-Asl, S.; Rehak, P.; Král, P.; Megaridis, C. M.; Shahbazian-Yassar, R.; Shokuhfar, T. Assessment of Pressure and Density of Confined Water in Graphene Liquid Cells. *Advanced Materials Interfaces* **2020**, *7*, 1–10.

(42) Yuk, J. M.; Kim, K.; Alemán, B.; Regan, W.; Ryu, J. H.; Park, J.; Ercius, P.; Lee, H. M.; Alivisatos, A. P.; Crommie, M. F.; Lee, J. Y.; Zettl, A. Graphene veils and sandwiches. *Nano Letters* **2011**, *11*, 3290–3294.

(43) Wu, H.-L.; Kuo, C.-H.; Huang, M. H. Seed-Mediated Synthesis of Gold Nanocrystals with Systematic Shape Evolution from Cubic to Trisoctahedral and Rhombic Dodecahedral Structures. *Langmuir* **2010**, *26*, 12307–12313.

(44) Elliot, A. J.; McCracken, D. R. Computer modelling of the radiolysis in an aqueous lithium salt blanket: Suppression of radiolysis by addition of hydrogen. *Fusion Engineering and Design* **1990**, *13*, 21–27.

(45) El Omar, A. K.; Schmidhammer, U.; Rousseau, B.; Laverne, J.; Mostafavi, M. Competition reactions of H2O•+ radical in concentrated Cl- aqueous solutions: Picosecond pulse radiolysis study. *Journal of Physical Chemistry A* **2012**, *116*, 11509–11518.

(46) Karnatak, R. C.; Esteva, J. M.; Dexpert, H.; Gasgnier, M.; Caro, P. E.; Albert, L. X-ray absorption studies of CeO2, PrO2, and TbO2. I. Manifestation of localized and extended f states in the 3d absorption spectra. *Physical Review B* **1987**, *36*, 1745–1749.

(47) Löble, M. W. *et al.* Covalency in lanthanides. An X-ray absorption spectroscopy and density functional theory study of LnCl6x- (x = 3, 2). *Journal of the American Chemical Society* **2015**, *137*, 2506–2523.

(48) Park, J.; Koo, K.; Noh, N.; Chang, J. H.; Cheong, J. Y.; Dae, K. S.; Park, J. S.; Ji, S.; Kim, I. D.; Yuk, J. M. Graphene Liquid Cell Electron Microscopy: Progress, Applications, and Perspectives. *ACS Nano* **2021**, *15*, 288–308.

(49) Chen, Q.; Smith, J. M.; Park, J.; Kim, K.; Ho, D.; Rasool, H. I.; Zettl, A.; Alivisatos, A. P. 3D Motion of DNA-Au Nanoconjugates in Graphene Liquid Cell Electron Microscopy. *Nano Letters* **2013**, *13*, 4556–4561.

(50) LaVerne, J. A.; Tandon, L. H 2 and Cl 2 production in the radiolysis of calcium and magnesium chlorides and hydroxides. *Journal of Physical Chemistry A* **2005**, *109*, 2861–2865.

(51) Schwarz, H. A. The Effect of Solutes on the Molecular Yields in the Radiolysis of Aqueous Solutions. *Journal of the American Chemical Society* **1955**, *77*, 4960–4964.

(52) Pastina, B.; Laverne, J. A.; Pimblott, S. M. Dependence of Molecular Hydrogen Formation in Water on Scavengers of the Precursor to the Hydrated Electron. *Journal of Physical Chemistry A* **1999**, *103*, 5841–5846.

(53) Massover, W. H. Electron beam-induced radiation damage: The bubbling response in amorphous dried sodium phosphate buffer. *Microscopy and Microanalysis* **2010**, *16*, 346–357.

(54) Dunn, G.; Adiga, V. P.; Pham, T.; Bryant, C.; Horton-Bailey, D. J.; Belling, J. N.; Lafrance, B.; Jackson, J. A.; Barzegar, H. R.; Yuk, J. M.; Aloni, S.; Crommie, M. F.; Zettl, A. Graphene-Sealed Flow Cells for in Situ Transmission Electron Microscopy of Liquid Samples. *ACS Nano* **2020**, *14*, 9637–9643.

(55) Kestin, J.; Khalifa, H. E.; Correia, R. J. Tables of the dynamic and kinematic viscosity of aqueous NaCl solutions in the temperature range 20–150 °C and the pressure range 0.1–35 MPa. *Journal of Physical and Chemical Reference Data* **1981**, *10*, 71–88.